Investigating chaotic wake dynamics past a flapping airfoil and the role of vortex interactions behind the chaotic transition

Chandan Bose, and Sunetra Sarkar

Articles you may be interested in

Influence of coherent structures on the evolution of an axisymmetric turbulent jet
Physics of Fluids **30**, 035109 (2018); 10.1063/1.5019668

Statistical features of rapidly rotating decaying turbulence: Enstrophy and energy spectra and coherent structures
Physics of Fluids **30**, 045103 (2018); 10.1063/1.5018346

Aerodynamic heating in transitional hypersonic boundary layers: Role of second-mode instability
Physics of Fluids **30**, 011701 (2018); 10.1063/1.5005529

Referee Acknowledgment for 2017
Physics of Fluids **30**, 010201 (2018); 10.1063/1.5022671

The regimes of twin-fluid jet-in-crossflow at atmospheric and jet-engine operating conditions
Physics of Fluids **30**, 025101 (2018); 10.1063/1.5010362

Flow dynamics in a variable-spacing, three bluff-body flowfield
Physics of Fluids **30**, 025105 (2018); 10.1063/1.5001943

Investigating chaotic wake dynamics past a flapping airfoil and the role of vortex interactions behind the chaotic transition

Chandan Bose[1] and Sunetra Sarkar[2,a)]

[1]*Department of Applied Mechanics, Indian Institute of Technology Madras, Chennai 600036, India*
[2]*Department of Aerospace Engineering, Indian Institute of Technology Madras, Chennai 600036, India*

The present study investigates the complex vortex interactions in two-dimensional flow-field behind a symmetric NACA0012 airfoil undergoing a prescribed periodic pitching-plunging motion in low Reynolds number regime. The flow-field transitions from periodic to chaotic through a quasi-periodic route as the plunge amplitude is gradually increased. This study unravels the role of the complex interactions that take place among the main vortex structures in making the unsteady flow-field transition from periodicity to chaos. The leading-edge separation plays a key role in providing the very first trigger for aperiodicity. Subsequent mechanisms like shredding, merging, splitting, and collision of vortices in the near-field that propagate and sustain the disturbance have also been followed and presented. These fundamental mechanisms are seen to give rise to spontaneous and irregular formation of new vortex couples at arbitrary locations, which are the primary agencies for sustaining chaos in the flow-field. The interactions have been studied for each dynamical state to understand the course of transition in the flow-field. The qualitative changes observed in the flow-field are manifestation of changes in the underlying dynamical system. The overall dynamics are established in the present study by means of robust quantitative measures derived from classical and non-classical tools from the dynamical system theory. As the present analysis involves a high fidelity multi-unknown system, non-classical dynamical tools such as recurrence-based time series methods are seen to be very efficient. Moreover, their application is novel in the context of pitch-plunge flapping flight. *Published by AIP Publishing.* https://doi.org/10.1063/1.5019442

I. INTRODUCTION

The study of unsteady aerodynamics of flapping wings has attracted a considerable amount of research attention in the recent past in relation to the design of flapping wing Micro-Aerial Vehicles (MAVs) as their small size and maneuverability is ideally suited to provide a futuristic device for advance surveillance and reconnaissance missions.[1–4] The associated small length-scales and low speed regime result in a low Reynolds number flow, in which the unsteady vortical patterns need to be resolved. Consequently, a large number of studies have examined the unsteady flow-field focusing on fundamental flapping kinematics like pure plunging[5–8] or pure pitching.[9,10]

A variety of wake patterns have been observed behind a flapping airfoil for an increasing Strouhal number ($St_A = fA/U_\infty$, where f and A are the frequency and amplitude of the oscillation, respectively, and U_∞ is the free-stream velocity). Note that most studies in this genre consider a pure plunging (and occasionally pure pitching) case, whereas studies with combined pitch-plunge kinematics are relatively rare. The reported wake patterns are commonly categorized as "drag-producing," "neutral," and "propulsive" wakes. The "drag producing wake" gives a momentum deficit streamwise velocity profile and the "propulsive" wake gives a jet-like velocity profile, which are characterized by Kármán and reverse Kármán vortex streets, respectively.[5,9] When St_A is further increased, the spatial symmetry of the wake pattern is lost resulting in a deflected vortex street which also indicates a nonzero average lift.[6,11–13] However, the periodicity of the wake is still retained in this regime. Eventually, with a further increase in St_A, the flow-field loses its periodic structure.

In flow-field past periodically flapped airfoils, observation of aperiodicity as has been reported in a number of studies[7,14–18] is very interesting. Some of them establish aperiodicity in the dynamics using qualitative pictures of the flow-field that show no repeatability or correlation in the vortex structures in the consecutive cycles;[14,19] in these studies, the authors have presented (for a combination of pitch-plunge flapping) phase averaged vorticity snap shots, obtained from soap-film experiments that show irregular and blurry patterns. Other studies focus on isolating some output measures of interest, like instantaneous velocity fields or aerodynamic loads to monitor the transition of the flow-field to aperiodicity (and chaos).[7,15,20] Aperiodicity was demonstrated through the time histories of such quantities; however, no rigorous quantitative tests based on dynamical systems theory were undertaken to establish the dynamics. Among them, Lewin and Haj-Hariri[7] and Ashraf, Young, and Lai[15] reported a quasi-periodic (QP) route to chaos for a plunging airfoil, whereas Blondeaux, Guglielmini, and Triantafyllou[20] observed the same for hovering kinematics. The latter study further observed a phase-locking scenario and commented on the airfoil behavior by

analyzing the Fourier spectra of the loads. In another recent study, Badrinath, Bose, and Sarkar[21] have discovered an intermittency route to chaos in a plunging airfoil and provided conclusive quantitative proofs to establish the presence of intermittency in the dynamics. The onset of aperiodicity in the amplitude-frequency parameter plane (for both pure plunging and pure pitching airfoils) has been reported by Kozłowski and Kudela[16] and Deng *et al.*[18] Martín-Alcántara *et al.*[17] and Deng *et al.*[18] had presented the varying pattern of the propulsive efficiency as the flow-field transitions to chaos and connected the optimum efficiency regime to the onset of chaos.

Please note that all the prior studies discussed above are for two-dimensional flow-fields and the same will be considered in the present analysis as well. Also, it is worth emphasizing that earlier analyses do not examine the underlying vortex interactions in their full complexity that are responsible to make the flow-field aperiodic when the flapping body itself is driven periodically nor did they follow the behavior from a dynamical perspective. These are the main focal points of the present research. It is of considerable interest to identify the role of the fundamental vortex interaction mechanisms behind the chaotic transition, as this can help understand the physics behind the qualitative changes observed in the flow-field. The key contribution of the present study is two-fold: (i) to identify the transition route to chaos by establishing the dynamics using robust quantitative measures derived from the flow field and (ii) to systematically unravel the underlying vortex interactions that trigger the unsteady flow-field to transition from periodicity to chaos.

For the first part of the objective, an array of flow-field quantities such as the streamwise velocity profile, vorticity, correlation of the vorticity field, phase averaged vorticity contours, and the aerodynamic loads is used to derive robust quantitative dynamical measures. Along the transition route, three distinct flow dynamics (periodic, quasi-periodic, and chaotic) are observed in the near-field wake. We rigorously substantiate the observed flow-field behavior into different dynamical states using tools from the dynamical systems theory. Once their existence is established through the said measures, the detailed vortex interactions that trigger these distinct dynamical states are investigated subsequently.

In the second part, the role of the leading edge vortices (LEVs) behind the flow-field transition has been found to be crucial. It is well known that natural fliers exploit the generation of the LEVs to augment their aerodynamic loads through the dynamic stall phenomenon.[22] The contribution of leading edge separation in the wake formation was investigated numerically by Lewin and Haj-Hariri[7] and later experimentally by Lua *et al.*[23] The topology of the leading-edge separation primarily depends on the reduced frequency (κ) as well as on the dynamic plunge velocity (κh). Lewin and Haj-Hariri[7] observed that for low values of κ, the primary LEV separates and advects downstream which is often followed by an interaction with the main trailing edge vortex (TEV). The LEV can either interact constructively with the TEV by reinforcing it or destructively by attenuating it.[24,25]

Lewin and Haj-Hariri[7] further observed that for high values of κ, often the LEV is not shed or advected downstream but gets stretched and dissipated by the nascent LEV of the

following stroke, especially in the aperiodic transition regime. The LEVs are also seen to circumnavigate the leading edge to reach the other side of the airfoil at high κ and κh values. However, for low κ and high κh cases, the leading-edge behavior in the aperiodic transition regime is still not well understood. This parametric regime is the subject of consideration in the present study. The near-field behavior is analyzed at a low value of $\kappa = 2$ as amplitude h is varied to a high κh regime. In order to distinguish between the periodic and the aperiodic regimes and to isolate the trigger for aperiodicity, the flow-field vortex interactions are analyzed in the light of fundamental 2D interaction mechanisms formerly recognized in the literature.[26,27] The contribution of LEVs is found to be crucial in the development of aperiodicity; in fact, the leading edge separation acts as the first trigger for aperiodicity. Its formation and separation happen in an irregular (aperiodic) manner that affects any subsequent regular formation of vortex structures. This includes LEV-TEV interactions as well as interactions with other existing vortices. The vortex patterns are presented in terms of the Lagrangian Coherent Structures (LCSs)[28] along with the vorticity contours. The LCSs are identified by computing Finite Time Lyapunov Exponent (FTLE) ridges[29] that explain the vortex interactions more clearly.

The remainder of the present paper consists of the following sections: Sec. II discusses the computational methodology. In Sec. III, the flow structures have been categorized to three distinct dynamics: periodic, quasi-periodic, and chaotic with the help of robust dynamical tools using direct flow measures. The fundamental vortex mechanisms have been studied in the near-field wake to understand their effect in the far-field and their contribution to the transition in the flow periodicity in Sec. IV. Finally, the paper ends with concluding remarks in Sec. V.

II. COMPUTATIONAL METHODOLOGY

A. Flapping kinematics

A sinusoidally pitching-plunging NACA 0012 airfoil in an incompressible flow has been considered for the present investigation. The flow past an NACA 0012 airfoil has been studied extensively in the existing literature and the flapping wake dynamics have been reported for both numerical[15,30–32] and experimental investigations.[5,9,33,34] Moreover, this symmetric profile falls in the optimal range of thickness to generate maximum time averaged thrust coefficient and propulsive efficiency in the concerned parametric regime of the present study.[35] Specifically, in NACA 0012, the thickness provides the desired frontal area for combined pitching-plunging motion against which the low pressure leading edge vortex can generate an increased thrust.[36]

The kinematic equations are given by

$$y(t) = A \sin(2\pi ft), \quad \dot{y}(t) = 2\pi fA \cos(2\pi ft),$$
$$\bar{\alpha}(t) = \alpha \sin(2\pi ft), \quad \dot{\bar{\alpha}}(t) = 2\pi f \alpha \cos(2\pi ft). \quad (1)$$

The non-dimensional parameters are defined as follows: reduced frequency $\kappa = 2\pi fc/U_\infty$, non-dimensional amplitude $h = A/c$, and $Re = U_\infty c/\nu$, where f is the oscillation frequency, c is the chord length, A is the plunge amplitude, α is the pitch

amplitude, U_∞ is the free-stream velocity, and ν is the kinematic viscosity. A parametric analysis is performed here by varying h from moderate to high value ($0.5 \leq h \leq 1.25$) at $\kappa = 2$, $\alpha = 15°$, and $Re = 1000$. The choice of the present parameter values is inspired from the fact that natural flyers frequently operate at high amplitude and low frequency regimes to produce large leading edge vortices that augment the lift generation.

B. Governing equations and solver details

In the present study, the low Reynolds number flow is modeled by an incompressible Navier-Stokes (N-S) equation. The arbitrary Lagrangian Eulerian (ALE) method[37] is adopted for the solution of the N-S equation in a time varying computational domain where the radial basis function (RBF) interpolation method[38] caters the need of a moving mesh mechanism. The N-S equation is cast into ALE form as

$$\nabla \cdot \vec{u} = 0, \tag{2}$$

$$\frac{\partial \vec{u}}{\partial t} + [(\vec{u} - \vec{u}^m).\nabla]\vec{u} = -\nabla p/\rho + \nu\nabla^2\vec{u}. \tag{3}$$

Here, $\vec{u}$ is the velocity of the flow, $\vec{u}^m$ is the grid point velocity, p is the pressure, ρ is the fluid density, and ν is the kinematic viscosity.

The spatial and temporal discretizations, used in the present solver, are second order accurate. An implicit backward differencing scheme is used for the temporal discretization along with a maximum Courant number-based variable time stepping method. The PISO (pressure implicit with splitting of operator) algorithm[37] with a predictor step and three pressure correction loops has been used to couple the pressure and velocity equations. A preconditioned conjugate gradient (PCG) iterative solver is used to solve the pressure equation where a diagonal incomplete-Cholesky (DIC) method is used for pre-conditioning. A preconditioned bi-stab conjugate gradient (PBiCG) solver is used to solve the pressure-velocity coupling equation and a diagonal incomplete-LU (lower-upper) factorization method is used for preconditioning. The absolute error tolerance criteria for pressure and velocity are set to 10^{-6}. The simulations are performed using a finite-volume-based computational fluid dynamics (CFD) solver OpenFOAM®.[39] One can find an extensive validation of the solver in Bos's Ph.D. thesis.[40] Additionally, the flow solver is also validated in the present study both qualitatively and quantitatively with the existing results from the literature (see Sec. II D).

C. Computational domain and boundary conditions

A schematic of the circular computational domain with a radius of 25c, used in the simulations, is shown in Fig. 1(a). The size of the computational domain has been chosen such that it is large enough to make the boundary effects redundant.[40] Therefore, the present results are insensitive to increase in the domain size. A zero pressure gradient and a constant free-stream are considered at the inlet, whereas a zero velocity gradient and atmospheric pressure condition are imposed at the outlet. Besides, no slip and zero normal pressure gradient conditions are considered on the horizontal walls and the airfoil surface and the latter is considered to be a moving wall. The computational domain is discretized using unstructured

grids. Figure 1(b) shows a close-up view of the mesh around the airfoil. For a better visualization of the boundary layer discretization, the zoomed view of the mesh around the leading and trailing edges has been presented in Figs. 1(c) and 1(d), respectively. A grid independence test was performed by comparing the aerodynamic lift and thrust coefficients (C_l and C_t) using grids of different resolutions to finalize the mesh. The results of the grid convergence study are presented in Figs. 1(e) and 1(f) for C_l and C_t, respectively. It can be seen that the results with 400 grid points agree very well with that of 600 grid points on the airfoil for both C_l and C_t. Hence, the mesh with 400 grid points on the airfoil (containing 0.36×10^6 grid points in total) is chosen for further analysis.

D. Validation of the unsteady flow solver

The unsteady flow solver has been validated both qualitatively and quantitatively by comparing the results of present computations with earlier experimental studies available in the literature. The validation has been carried out for both pure plunging and pure pitching kinematics. The trailing edge wake patterns of a plunging airfoil obtained from the present computation have been compared with that of the dye flow visualization results of Jones *et al.*[6] Figures 2(a) and 2(b) show the comparison of wake vorticity contours for $\kappa = 3$ and $h = 0.2$ ($\kappa h = 0.6$). The present computational results corroborate the experimental results. A similar comparison is presented for a higher non-dimensional plunge velocity case using $\kappa = 12.5$ and $h = 0.12$ ($\kappa h = 1.5$) in Figs. 2(c) and 2(d). A deflected vortex street is observed for such high non-dimensional plunge velocities ($\kappa h > 1$). A close agreement between the computational and experimental flow patterns is seen in this case also.

Similarly for pure pitching cases, the numerically obtained vortex contours have been compared with the Laser Doppler Velocimetry (LDV) measurements performed by Koochesfahani.[9] The comparative study has been carried out for three different set of parameter values as follows: for $\kappa = 0.84$ and $\alpha = 4°$ [Figs. 3(a) and 3(b)] where an undulating Kármán vortex street is observed, for $\kappa = 3.1$ and $\alpha = 4°$ [Figs. 3(c) and 3(d)] where a 2P wake pattern is observed with double-wake structure, and for $\kappa = 6.7$ and $\alpha = 2°$ [Figs. 3(e) and 3(f)] where a neutral vortex street is observed. Thus the present results closely match the earlier experimental results for the pure pitching cases as well.

Quantitative validation of the solver has been obtained for both pure plunging and pure pitching kinematics by comparing the aerodynamic loads obtained from the present computations with the earlier experimental results of Cleaver, Wang, and Gursul[41] and Mackowski and Williamson,[42] for pure plunging and pure pitching, respectively. Cleaver, Wang, and Gursul[41] have performed force measurements for a NACA 0012 airfoil plunging with sinusoidal kinematics with various amplitudes and frequencies in a water tunnel at $Re = 10\,000$. Please note that a solver validated at a higher Reynolds number would be valid in the lower range as well since a higher Re case requires a better grid resolution to capture the larger gradients. Figure 4(a) shows the comparison of the time-averaged drag coefficients for different reduced frequencies (κ) for plunging amplitude, $h = 0.20$. The present computational results show
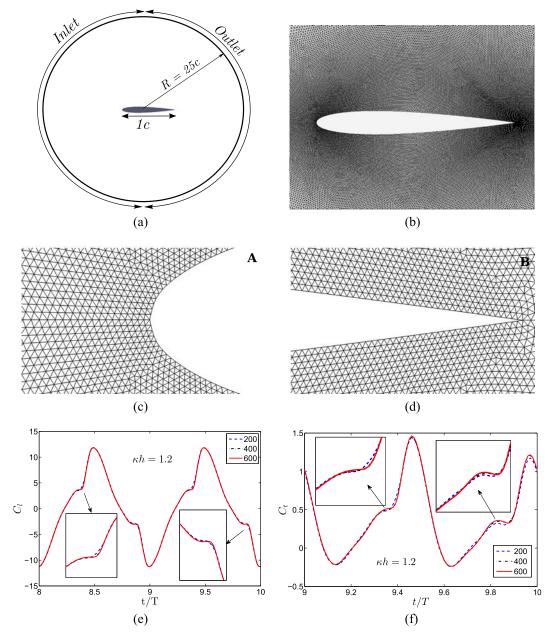
FIG. 1. (a) Computational domain for the analysis (not to scale), (b) a close-up view of the computational grid around the airfoil. Zoomed view of the mesh around (c) the leading edge (region "A") and (d) the trailing edge (region "B"). Grid independence results for (e) C_l and (f) C_t; legend indicates the number of points on the airfoil surface.
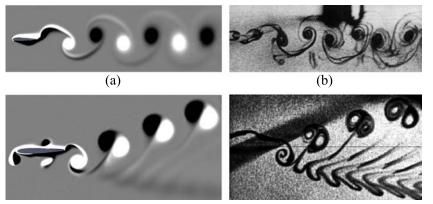

FIG. 2. A comparison of the vorticity contours from the present computation (left) with the dye flow visualization results obtained by Jones et al.[6] (right) for a plunging airfoil with kinematic parameters: $\kappa h = 0.6$, $h = 0.2$ (top) and $\kappa h = 1.5$, $h = 0.12$ (bottom). [Experimental frames has been reproduced with permission from Jones et al., "Experimental and computational investigation of the Knoller-Betz effect," AIAA J. 36(7), 1240 (1998).]
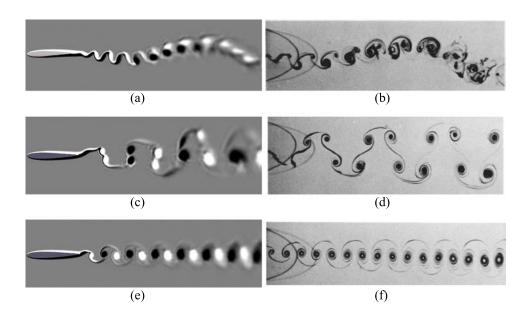
FIG. 3. A comparison of the vorticity contours from the present computation (left) with the flow visualization results obtained by Koochesfahani[9] using LDV (right) for a pitching airfoil with kinematic parameters: $\kappa = 0.84$, $\alpha = 4°$ (top), $\kappa = 3.1$, $\alpha = 4°$ (middle), and $\kappa = 6.7$, $\alpha = 2°$ (bottom). [Experimental frames has been reproduced with permission from M. M. Koochesfahani, "Vortical patterns in the wake of an oscillating airfoil," AIAA J. **27**, 1200–1205 (1989). Copyright 1989 American Institute of Aeronautics and Astronautics, Inc.]

a good agreement with the experimental results. Figure 4(b) compares the computed thrust coefficients for pure pitching cases with pitch amplitude 2° and $0 \leq \kappa \leq 7$ with the experimental results of Mackowski and Williamson.[42] It is seen that the computed coefficients reasonably conform with the experimental results in this case as well. However, small deviation is noticed at higher κ values for both pitching and plunging kinematics which could possibly be attributed to the higher Re $(O(10^4))$ used for the above experiments. It should be noted that in the present study κ is chosen as 2, at which the results from the present solver match the experimental results well. After the validation of the unsteady flow solver, the same is used to explore the flow physics in the concerned parametric range.

E. Flow-field representation in terms of the Lagrangian coherent structures

The near-field flow structures become quite complicated at high flapping amplitudes as the flow-field loses periodicity.

Hence, Lagrangian Coherent Structures (LCSs) are tracked along with the vorticity contours to capture the intricate vortex interactions in detail. Haller et al.[28,43] were the first to introduce the framework of LCSs into the realm of fluid dynamics to detect coherent structures which are an essential part of the unsteady flows. LCSs are defined as finite-time attracting and repelling material surfaces in the Lagrangian fluid motion governing the flow or mass transport. They are also considered as one kind of invariant manifold representing dynamic transport barriers in the flow. It was proposed by Haller[29] that ridges of the finite-time Lyapunov exponent (FTLE) can be considered as heuristic indicators of hyperbolic (i.e., repelling and attracting types) LCSs. The attracting material lines are named as unstable manifolds which contain the information of the past, and the repelling material lines are termed as stable manifolds which contain the future information. Very recently, it has also been used for investigating the flow past flapping airfoils.[44–49] In this paper, the *attracting* LCSs are computed as the backward FTLE ridges based on the Cauchy-Green tensor in the vector field using the algorithm
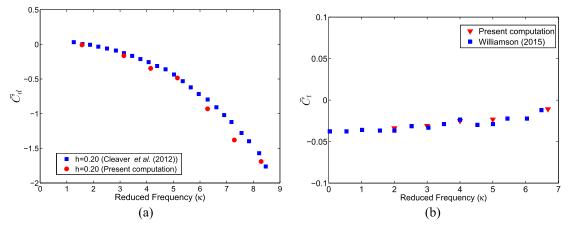

FIG. 4. (a) Validation for plunging: comparison of drag coefficients with the experimental measurements of Cleaver et al.[41] for a plunging airfoil with $h = 0.2$, $Re = 10\,000$; (b) validation for pitching: comparison of thrust coefficients with the experimental measurements of Mackowski and Williamson[42] for a pitching airfoil with $\alpha = 2°$, $Re = 12\,000$.

developed by Onu *et al.*[50] Using the LCSs, the exact vortex boundaries as well as the time-dependent separation and reattachment of the leading-edge vortices are studied with high resolution.

III. DYNAMICAL SIGNATURE OF THE NEAR-FIELD WAKE

The dynamical signature of various flow-field variables are investigated in this section. The variables chosen here include flow-field quantities like instantaneous vorticity and velocity as well as derived quantities like aerodynamic loads. We emphasize that the use of classical tools such as Lyapunov exponent and fractal dimension for the present large order system could be tedious. They require long time histories of the concerned field variables (generating long time histories from a high fidelity N-S-based solver is computationally expensive) and often work better for low order or analytical models.[51,52] On the other hand, dynamical time series tools such as those based on the property of recurrence[53] are much more efficient for time data analysis. They do not need very long time histories unlike the classical tools[54,55] and provide
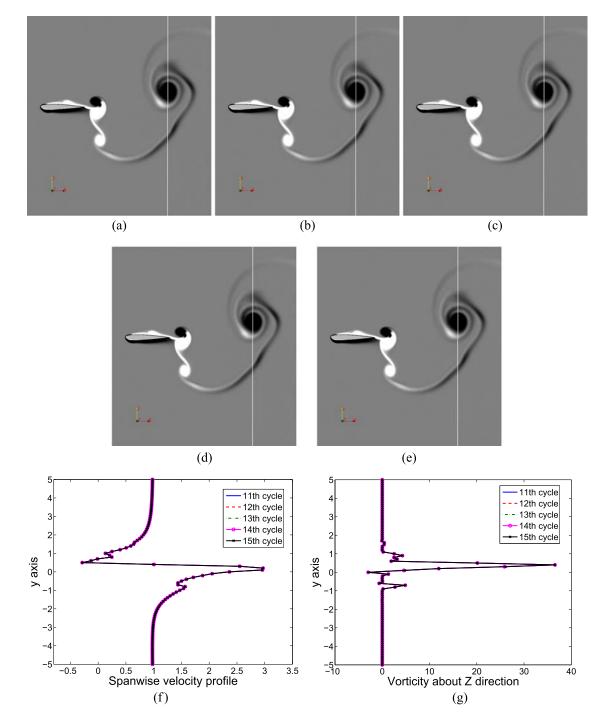

FIG. 5. Comparison of velocity (u_x) and vorticity (Ω_z) profiles for $h = 0.5$ (periodic regime). (a) $t/T = 11$. (b) $t/T = 12$. (c) $t/T = 13$. (d) $t/T = 14$. (e) $t/T = 15$. (f) Streamwise velocity profile. (g) Vorticity profile about the Z direction.

robust quantitative measures to pinpoint the onset of changes in the respective dynamical states. These tools are employed in the present study. Note that the use of nonlinear time series tools is novel in the context of flapping flow-field and provides a fresh perspective to the investigation.

A. Vorticity contours and instantaneous flow-field measures

As already mentioned, with increase in the plunge amplitude, qualitatively different wake patterns are observed in the near-field. Three qualitatively different patterns have been observed in the present study as the control parameter (h) changes. The first one is a periodic wake for which the vorticity

contours replicate each other exactly from cycle to cycle. The second is a quasi-periodic flow in which the wake pattern takes a marginal detour in consecutive periods giving rise to a large change after a few cycles which eventually returns to the neighborhood of the initial topology again but never exactly to the same position. The third is completely aperiodic or chaotic flow where there is no correlation in the flow topology between any two consecutive cycles. The flow-field behavior during periodic, quasi-periodic, and chaotic dynamics has been presented for 5 *typical* consecutive cycles ($t/T = 11$–$t/T = 15$) in order to observe the changes from one cycle to another without loss of generality. This is to monitor if the changes are minute or significant from one cycle to the next over a finite number of cycles. Though presented for 5 cycles only, it is
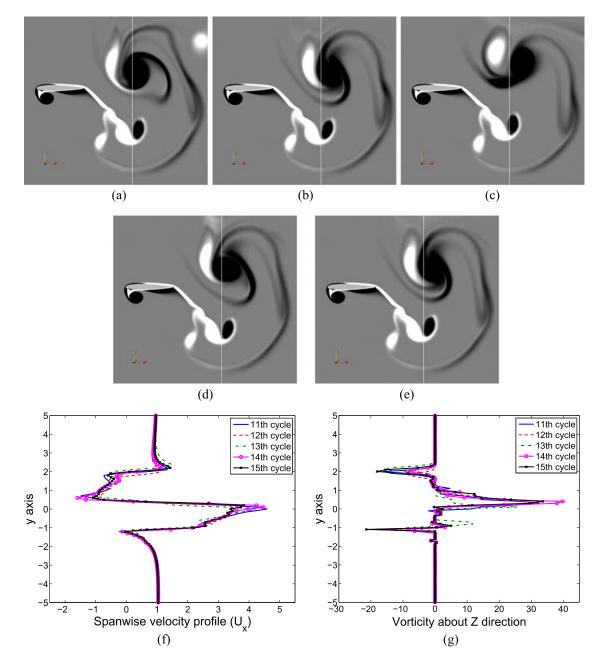

FIG. 6. Comparison of velocity (u_x) and vorticity (Ω_z) profiles for $h = 0.85$ (quasi-periodic regime). (a) $t/T = 11$. (b) $t/T = 12$. (c) $t/T = 13$. (d) $t/T = 14$. (e) $t/T = 15$. (f) Streamwise velocity profile. (g) Vorticity profile about the Z direction.

to be noted that the simulations were carried out for about 75 periodic cycles for every parameter value, in order to confirm if the transient state has passed and the flow-field reflects the actual system dynamics. Even after a sufficiently long period of time, no change in the vortex interaction mechanisms in the near-field for periodic as well as quasi-periodic regimes is observed. In the quasi-periodic regime, the vortex cores are seen to be shifted slowly from one cycle to other until they occupy a very different space far from their initial position and thereafter again coming back to the proximity of their previous position in the subsequent cycles. In the chaotic regime, the flow-field is seen to be completely unpredictable from cycle to cycle; hence, no similarity was found in the vortex interactions in the entire simulation period.

The periodic flow-field is presented in Figs. 5(a)–5(e) for $h = 0.5$ in terms of the vorticity contours for five consecutive cycles and they are seen to be identical. The interactions between LEVs and TEVs are periodic and are mirror images in two consecutive half cycles; a reverse von Kármán wake pattern (periodic) is observed in the trailing wake. The vortex interaction mechanisms behind the periodic behavior will be discussed in detail later in the paper. The streamwise velocity (u_x) and the vorticity (Ω_z) profiles (at a fixed vertical plane intersecting the core of the primary anti-clockwise vortex in the near-field) are shown for 11th–15th cycles in Figs. 5(f) and 5(g), respectively. As expected, the u_x and the Ω_z profiles remain identical for different cycles conforming to the periodic signature of the flow. The flow-field remains periodic up to $h \leq 0.8$; however, the wake undergoes a deflection beyond $h \geq 0.7$, thus loosing its spatial symmetry.

For $h > 0.8$, the flow-field looses its periodicity and changes qualitatively. The wake patterns for $h = 0.85$ are presented in Figs. 6(a)–6(e) in terms of the vorticity contours for five consecutive cycles (11th–15th cycles). The periodicity of the flow-field is lost due to a gradual time delay (phase-shifting) in the behavior of the main leading-edge structures that affect the LEV-TEV interactions. Comparing the flow-fields at the same phase of five consecutive cycles, it is seen that the position of the vortex cores shifts a little from cycle to cycle but it stays in the neighborhood. The u_x and Ω_z profiles have been plotted for the 11th–15th cycles in Figs. 6(f) and 6(g), respectively. Unlike the periodic case, they do not coincide with each other but deviate in small margins from one cycle to another being in the neighborhood, which is a signature of quasi-periodicity. To appreciate this better, the near-field vortex structures of the 12th–15th cycles are compared one by one with that of the 11th cycle in Figs. 7(a)–7(d). This also suggests by what measure the flow-field in the consecutive cycles deviates from the starting cycle (11th) and if the flow-field shows any tendency to come back to it. It is evident from these comparative frames that the vortex structures remain in the neighborhood in consecutive time-cycles but they do not come back exactly to the earlier position. This confirms a deviation from periodicity and marks the quasi-periodic state.
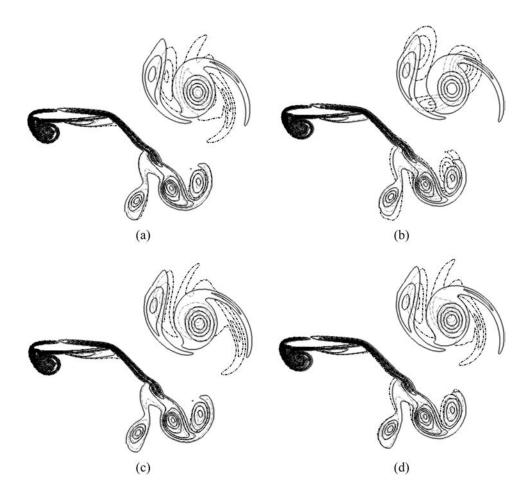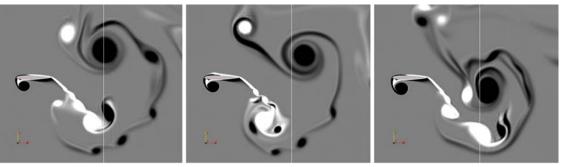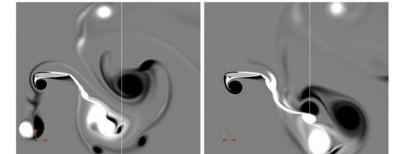

FIG. 7. Comparison of near-field vortex structures in the quasi-periodic regime at $h = 0.85$. (a) 11th VS 12th cycle. (b) 11th VS 13th cycle. (c) 11th VS 14th cycle. (d) 11th VS 15th cycle.

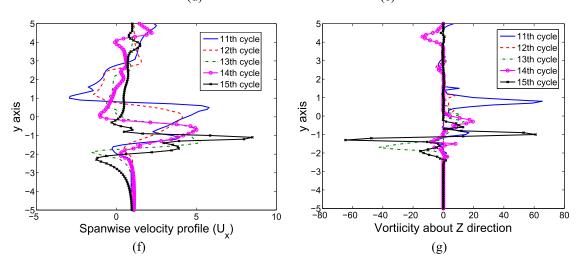FIG. 8. Comparison of velocity (u_x) and vorticity (Ω_z) profiles for $h = 1.25$ (chaotic regime). (a) $t/T = 11$. (b) $t/T = 12$. (c) $t/T = 13$. (d) $t/T = 14$. (e) $t/T = 15$. (f) Stream-wise velocity profile. (g) Vorticity profile about the Z direction.

As the amplitude is increased further to $h = 1.25$, the flow-field becomes chaotic. The flow patterns, presented in Figs. 8(a)–8(e) for five consecutive cycles, show that there is no similarity in the vortex structures between any two cycles (consecutive or otherwise). Very complex vortex interactions are seen in the flow-field and it is completely unpredictable. There is no correlation between the vortex structures in different cycles which is confirmed by the streamwise velocity and the vorticity profiles presented in Figs. 8(f) and 8(g), respectively.

So far, the categorization of the near-field flow dynamics into three distinct flow patterns (periodic, quasi-periodic, and chaotic) has been done based on the qualitative flow patterns and the instantaneous flow-field measures such as velocity and vorticity profiles. In the rest of this section, the phase averaged vorticity contours and the correlation of the vorticity fields

are used; and subsequently, in Sec. III D, robust time series tools from dynamical systems theory are used to establish the changes in the flow-field conclusively.

B. Phase averaged vorticity contours

Averaging of the vorticity snapshots over the same time interval results in a crisp image in the periodic regime since the wake pattern repeats itself exactly in every cycle. On the contrary, it produces a blurry pattern when there is no correlation in the flow-field during chaos.[14] The phase averaged vorticity contours are presented for different h values in Fig. 9. Figure 9(a) shows a crisp pattern indicating a periodic flow-field at $h = 0.5$, while a blurred pattern is seen in Fig. 9(c) indicating a chaotic flow-field at $h = 1.25$. The phase averaged vorticity contour for $h = 0.85$, as seen in Fig. 9(b), is neither
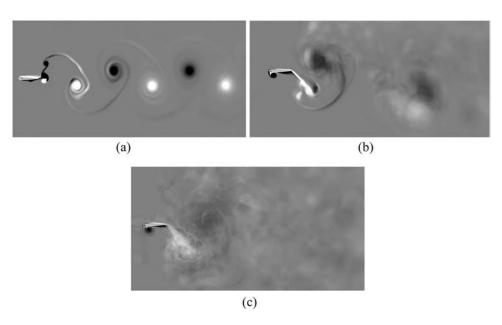
FIG. 9. Comparison of phase averaged vorticity contours. (a) h = 0.5. (b) h = 0.85. (c) h = 1.25.

as crisp as the periodic case nor as blurred as the chaotic case. It corresponds to the transition phase. This can be attributed to the quasi-periodic dynamics as the flow structures neither recur in every cycle nor deviate as drastically as the chaotic regime, but they remain in the neighborhood.

C. Correlation of vorticity field

A quantitative measure of periodicity can be obtained by computing the correlation of the vorticity field. This is defined below in Eq. (4) for different time instants (t) with respect to a reference time (t_{ref}). We compute this over the near-field wake region containing all the primary vortex structures over a rectangular region of size ($9.8c \times 14c$) behind the airfoil (symmetrically placed at a distance of $0.2c$ from the trailing edge). The region is discretized into n evenly spaced grid points and the vorticity field is then interpolated on to them. The correlation coefficient (ρ) of the vorticity field is defined as follows:

$$\rho(t) = \frac{\sum_{i=1}^{n} \left(\Omega_i(t) - \overline{\Omega}(t) \right) \left(\Omega_i(t_{\text{ref}}) - \overline{\Omega}(t_{\text{ref}}) \right)}{\sqrt{\sum_{i=1}^{n} \left(\Omega_i(t) - \overline{\Omega}(t) \right)^2} \sqrt{\sum_{i=1}^{n} \left(\Omega_i(t_{\text{ref}}) - \overline{\Omega}(t_{\text{ref}}) \right)^2}}.$$

$$(4)$$

In Eq. (4), $\Omega(t)$ is the vector containing the vorticity values at the n grid points at a time instant t and $\overline{\Omega}(t)$ is the spatial average of the vorticity field ($\Omega(t)$) calculated over the n grid points and thus is a function of time. The correlation coefficient $\rho(t)$ takes values from -1 to 1. When the vorticity field at any t is exactly identical to that of t_{ref}, $\rho(t)$ would become "1." Similarly, $\rho(t)$ would become "-1" when the vorticity field is of the same magnitude but of opposite sign; it would encounter values around "0" when the vorticity field is strongly dissimilar to that of t_{ref}, which indicates no correlation. For quasi-periodic dynamics, the loss of correlation is manifested through small values but not around "0." This is in accordance with the standard meaning of correlation which is a measure of linear dependence between two quantities. The time history of $\rho(t)$ for a periodic wake pattern would also

be periodic. Since the vorticity field repeats periodically, the maximum amplitude of $\rho(t)$ would be close to unity. On the other hand, it would be close to zero for a chaotic flow-field. The correlation time history plots for different h are presented in Fig. 10 considering $t_{ref} = 20T$. Based on the earlier definition of $\rho(t)$, the periodic, quasi-periodic, and chaotic patterns are easily recognizable at $h = 0.5$, $h = 0.85$, and $h = 1.25$, respectively.

D. Dynamical analysis with nonlinear time series tools

The flow transition can be efficiently analyzed using chaos theory[56] by deriving a finite set of modes or basis to separate the spatio-temporal description of the flow-field. However, the use of classical chaos theory to establish the chaotic transition in the flow-field in an infinite order system or in a large order system like the one in the present study poses a number of challenges.[52] Besides, an accurate estimate of classical topological measures like largest Lyapunov exponent or fractal dimension demands a long time history of the concerned field variable. Therefore, they are more applicable to the lower order systems. In the present study, these challenges are bypassed and the overall dynamics are resolved using the relatively unconventional nonlinear time series tools (in addition to the classical tools like frequency spectra, phase-space, Poincaré section, etc.) which are efficient even for short time histories and robust.

The dynamical evolution of the aerodynamic lift coefficient (C_l) is used to investigate different attractors present in the system at different h values. Additionally, the time history of the streamwise velocity (U_x) is analyzed to establish the chaotic flow dynamics. C_l and U_x have been chosen to carry out the time series analyses as they are direct measures from the flow-field. The time histories of C_l for $h = 0.5$, 0.85, and 1.25 are presented in Figs. 11(a), 11(d), and 11(g), respectively. Figure 11(a) shows the constant amplitude regular oscillations characterizing the periodic dynamics, whereas a modulating oscillation can be seen in the quasi-periodic dynamics at
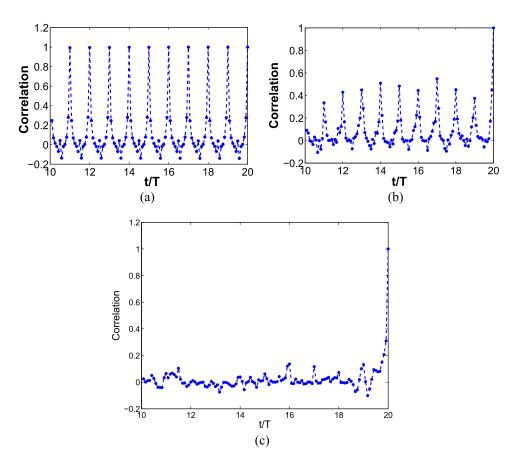
(a)

(b)

(c)

FIG. 10. Comparison of correlation coefficients of the vorticity fields. (a) h = 0.5. (b) h = 0.85. (c) h = 1.25.

$h = 0.85$ [Fig. 11(d)]. Contrastingly, the C_l time history is completely aperiodic at $h = 1.25$ [Fig. 11(g)]. It is to be noted that the high values of C_l generated in the chaotic regime can be attributed to the high amplitude of oscillations which manifest stronger dynamic stall vortices.

A phase-space behavior is more informative as attractors can be better visualized in the phase-space. Since C_l is a derived quantity from the flow-field, the derivative of C_l cannot be calculated directly, to use to construct the phase-space. Hence, time delay reconstruction of pseudo-phase space, based on Taken's embedding theorem,[57] is carried out from the scalar time series of C_l to reveal the system attractors. The method of time delay involves obtaining a series of independent time-delayed vectors representing the system dynamics from a single time series data based on the optimum time delay and the minimum embedding dimension of the system. The reconstruction matrix (Y) can be expressed as $Y = [C_l(t) \; C_l(t + \tau) \; C_l(t + 2\tau) \cdots C_l(t + (d - 1)\tau)]$, where τ and d are the optimum time delay and minimum embedding dimension, respectively. The optimum time delay is determined using the method of mutual information[58] by calculating the average mutual information between the original and the time delayed vectors. The minimum embedding dimension is computed using the method of false neighborhood[59] by checking whether the distance between two points in the phase space is invariant with increasing dimension. The reconstructed phase portraits for C_l at $h = 0.5, 0.85,$ and 1.25 are presented in Figs. 11(b), 11(e), and 11(h), respectively. It is to be noted that an embedding dimension of 5 was required for an accurate reconstruction of the phase space. However, it is projected on to a

three-dimensional space for the sake of visualization. The phase portrait at $h = 0.5$ represents a closed attractor characterizing the periodic nature of the flapping motion. However, it takes the shape of a dense toroidal structure at $h = 0.85$, which is characteristic of quasi-periodic dynamics. Finally, a chaotic attractor is observed at $h = 1.25$ where the phase space is completely filled by the trajectories. To support this argument, the $C_l - C_d$ phase portraits are also presented for $h = 0.5, 0.85,$ and 1.25 in Figs. 11(c), 11(f), and 11(i), respectively, reflecting the same dynamics. The frequency spectra of the C_l time history are presented in Fig. 11(j). One can see that only one dominant frequency is present along with its super harmonics in the periodic regime at $h = 0.5$. Whereas, multiple non-harmonic peaks are seen at $h = 0.85$ depicting the quasi-periodic nature of the oscillation. Finally at $h = 1.25$, the frequency spectra becomes completely broad banded with a wide range of frequencies along with the forcing frequency which is indicative of a chaotic dynamics. U_x shows the same transition route. The existence of the chaotic attractor is also confirmed through the time series analysis of U_x in Figs. 12(a)–12(d). Note that the phase space [Fig. 12(c)] and the stroboscopic Poincaré section [Fig. 12(d)] do not represent a well-developed strange attractor; however, the short time history as well as the projected visualization of the phase-space onto a lower dimensional space might be the underlying reason.

These three qualitatively distinct regimes can be further distinguished conclusively through the visual representation of recurrence plots (RPs).[53,60] RPs can reveal the dynamical changes of any system even for a relatively short time series data which makes it useful for studies where large time signals
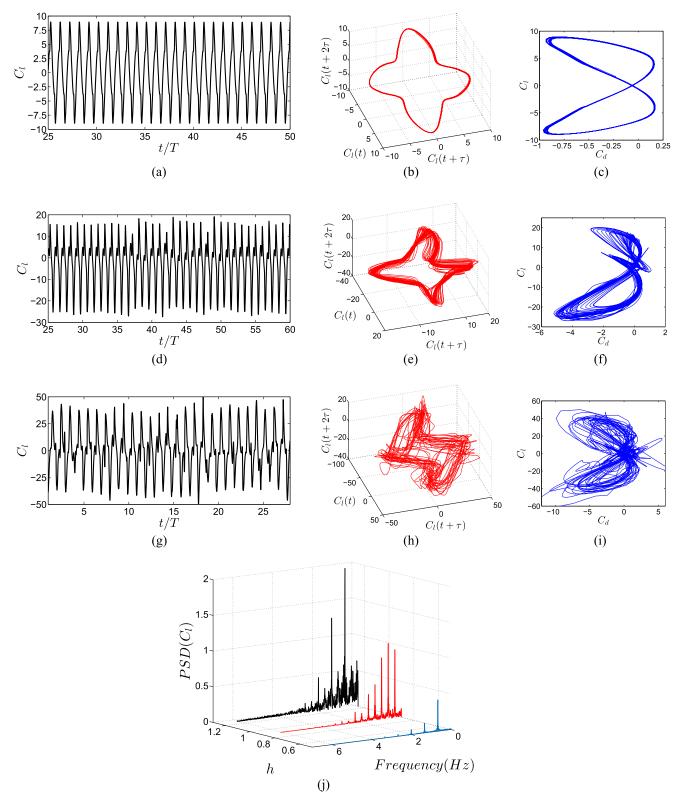
FIG. 11. Nonlinear time series analysis of lift co-efficient (C_l). (a) Time history of C_l at $h = 0.5$. (b) Phase space of C_l at $h = 0.5$. (c) $C_l - C_d$ phase plot at $h = 0.5$. (d) Time history of C_l at $h = 0.85$. (e) Phase space of C_l at $h = 0.85$. (f) $C_l - C_d$ phase plot at $h = 0.85$. (g) Time history of C_l at $h = 1.25$. (h) Phase space of C_l at $h = 1.25$. (i) $C_l - C_d$ phase plot at $h = 1.25$. (j) Frequency spectra of C_l.

are expensive to generate like the present one. Furthermore, any slight modulations in frequency and phase can be easily detected visually in contrast to conventional spectral analysis.[61] Recurrence plots (RPs) are constructed from a binary

recurrence matrix, $R_{i,j} = \Theta(\epsilon - ||x_i - x_j||)$, $i, j = 1, 2, 3, \ldots, N$, for a phase space with N points. Here, x_i is a point in the "d" dimensional phase space, Θ is the Heaviside step function, ϵ is a predefined threshold, and $||\cdot||$ indicates the L_2 norm. The
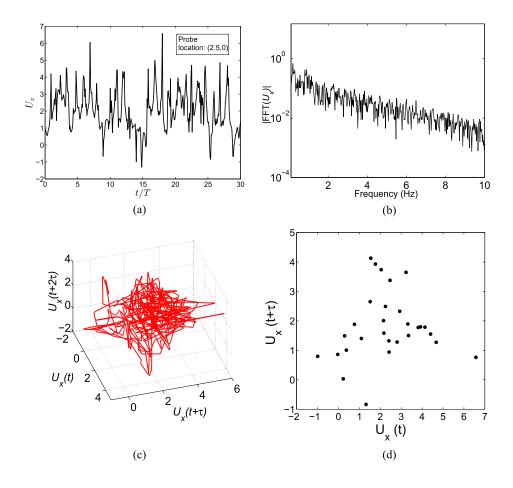
(a)

(b)

(c)

(d)

FIG. 12. Nonlinear time series analysis of streamwise velocity (u_x). (a) Time history of u_x. (b) Frequency spectra of u_x. (c) Reconstructed phase space of u_x. (d) Poincaré section of u_x.

graphical representation of RPs is sensible to the threshold ϵ; an optimal value of ϵ needs to be chosen to represent the accurate dynamics. In our calculation, ϵ is chosen to be at 10% of the diameter of the reconstructed phase space. The diameter refers to the distance between the two farthest points in the phase space. $R_{i,j}$ is considered to be zero if the distance between the two points x_i and x_j in the phase space is greater than ϵ, else it is equal to unity. The recurrence plot contains black and white points corresponding to ones and zeros of the recurrence matrix, respectively. The recurrence plots for the time histories of C_l corresponding to $h = 0.5$, 0.85, and 1.25 are plotted in Figs. 13(a)–13(c), respectively. Equally spaced diagonal lines parallel to the main diagonal in the RP reflect the

periodic dynamics at $h = 0.5$; see Fig. 13(a). On the other hand, the unequally spaced discontinuous diagonal lines parallel to the main diagonal in RP clearly distinguish the quasi-periodic dynamics from the periodic one at $h = 0.085$; see Fig. 13(b). The chaotic dynamics at $h = 1.25$ are characterized by very short broken lines and isolated dots in RP as can be seen in Fig. 13(c).

We have established the dynamical states through conclusive quantitative tests using the time series information of a flow-field quantity, U_x, as well as the aerodynamic load which is derived from the flow-field. Thus, a quasi-periodic route to chaos is identified and established in the unsteady flow-field using tools from the dynamical systems theory. In Sec. IV, we
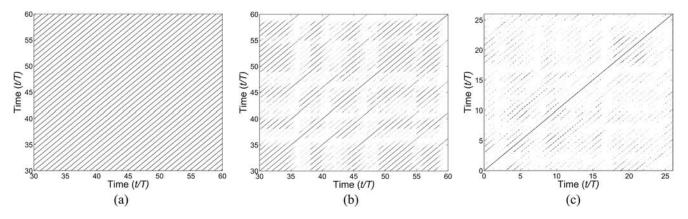

(a)

(b)

(c)

FIG. 13. Comparison of recurrence plots of C_l. (a) h = 0.5. (b) h = 0.85. (c) h = 1.25.

focus on the details of the unsteady flow-field and investigate the underlying vortex interaction mechanisms that lead to the dynamical transition.

IV. UNDERLYING VORTICITY DYNAMICS BEHIND THE TRANSITION

The qualitative changes in the dynamics of the wake are an outcome of diverse interactions among the main vortex structures. To the best of our knowledge, a detailed investigation of these interactions and their role behind the transition to aperiodicity in a flapping flow-field has not been reported in the existing literature.

In 2D, the interactions between two isolated vortices could be quite varied depending on whether they are of the same or opposite signs.[27] Their comparative strengths also play a crucial role. Here, two isolated vortices of opposite sense of rotation are called a couple and of same sense are called a pair. As any couple moves under its self-induced velocity field, a rectilinear translation motion is followed if both the counterparts are equally strong, and a rotational motion is observed if the counterparts have unequal strengths. In the latter case, the rotation takes place in the direction of the stronger vortex. On the other hand, two co-rotating vortices interact irreversibly through vortex pairing process and merge into a unique larger vortex structure. When their strengths are unequal, the weaker one gets merged partially with the stronger one. A detailed discussion on the behavior of counter-rotating and co-rotating vortices has been given by Leweke *et al.*[26] There exist a number of fundamental vortex interaction mechanisms in 2D which are relevant to the present case. They are outlined in the following and will be identified in the flapping flow-field as it transits through the different dynamical states.

- *Partial and complete merging*

Two co-rotating vortices of unequal strengths may undergo a *partial merging* upon collision. In this process, the weaker vortex is deformed and strained by the stronger one and *partially merge* with it. On the contrary, when two co-rotating vortices of equal or near-equal strengths collide, *complete merging* may happen to form a single stronger structure.[26]

- *Vortex splitting and shredding*

Additionally, splitting, shredding, or fission of vortices are also commonly observed. A single vortex can be split into multiple small vortices by the influence of nearby opposite sense vortices. This is known as *vortex splitting*.[62] In *vortex shredding*, systematic deformation and eventual shredding of a vortex takes place by which it can disappear in the presence of a stronger opposite sense vortex.[63]

- *Collisions of vortex couples and exchange of partners*

Collisions between two vortex couples may take place elastically or inelastically. In *elastic collisions*, the couples either undergo a head-on collision or collide symmetrically with respect to the bisector of the angle at which the

trajectories of the two couples' axes intersect.[27] *Elastic collision* results in *partner exchange* and two different couples result from this process. On the contrary, *inelastic collisions* are the non-symmetrical collisions and are often associated with a *vortex merging* or *splitting* phenomena. *Inelastic collision* of two couples having non-uniform strengths gives a vortex couple and two isolated vortices. Two couples may also collide over an isolated vortex in which the isolated vortex gets trapped between the couples and becomes part of one of them. Subsequently, an *inelastic collision* process may take place between the couples.
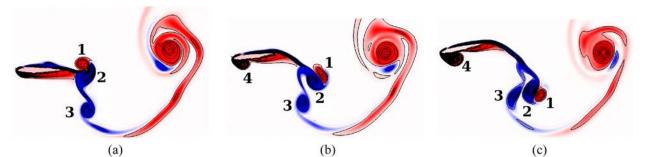
We identify these interactions in the context of periodic, quasi-periodic, and chaotic states in Subsections IV A–IV C and investigate on their role in making the flow-field periodic to aperiodic. Snapshots of the 2D unsteady field are presented in terms of the backward finite time Lyapunov exponent (FTLE) ridges[28,43] along with the corresponding vorticity contours.
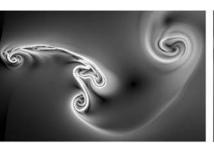
A. Periodic regime

In the periodic regime ($h = 0.5$), two isolated vortices having opposite sense of rotation appear in the wake periodically after each cycle in an organized manner and form a reverse Kármán vortex street. The near-field vorticity contours and the corresponding backward FTLE contours are presented sequentially in Figs. 14(a)–14(n) during the upstroke of a typical periodic cycle chosen for investigation (11th *cycle*) for $h = 0.5$.

At the start of the up-stroke [Fig. 14(a)], two clock-wise vortices "2" and "3" along with a comparatively weaker counter clock-wise vortex "1" (generated as a secondary vortex structure from the upper surface) are seen in the near-field. They were formed during the previous half-cycle (down-stroke) of the flapping motion. As the airfoil proceeds in its upstroke, vortices "1" and "2" form a couple of unequal strengths which traverses into a clock-wise circular arc due to its self-induced velocity dominated by the stronger "2" [Figs. 14(b) and 14(c)]. As the couple comes near "3," *partial merging* takes place between "2" and "3" resulting in a merged vortex "5" [Fig. 14(m)]. During the merging process, *vortex shredding* happens to "1" under the influence of the stronger counterpart "2." "5" would eventually advect towards downstream in the next half cycle. A LEV "4" [Fig. 14(b)] forms and grows [Figs. 14(c)–14(g)] during the up-stroke. At the end of the up-stroke, it gets shed at the trailing edge along with a secondary structure "6" and a trailing edge structure "7" [Fig. 14(m)]. The vortices "6," "4," and "7" undergo exactly similar interactions as that of "1," "2," and "3," respectively, in the next half-cycle and an isolated vortex similar but with a sense opposite to "5" is formed. This chain of vortex interactions is repeated periodically with the up- and down-stroke patterns being mirror images of each other. Overall, one isolated vortex is shed at the end of each stroke (half-cycle), and at the end of one full cycle, two vortices of opposite senses emerge. These two form the fundamental building block of an array of vortices with a counter clock-wise vortex above and a clock-wise vortex below the mean line, respectively, resulting in a periodic reverse Kármán street [Fig. 14(o)].

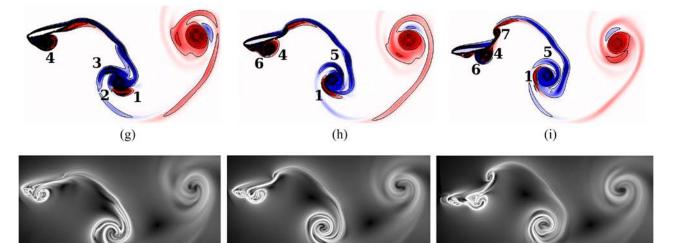As the plunge amplitude is increased to $h = 0.7$, the spatial symmetry of the wake is broken although the temporal
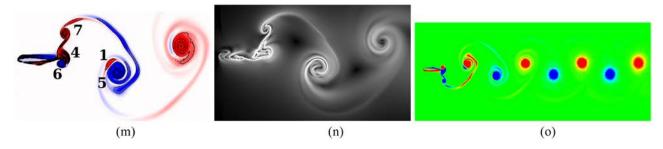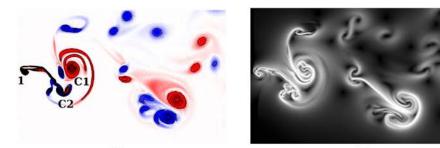
FIG. 14. Periodic regime: [(a)–(n)] The near-field vorticity dynamics (up-stroke of 11th *cycle*) and (o) symmetric reverse Kármán vortex street in the periodic regime at $h = 0.5$. (a) Vorticity contour at t/T = 10.00. (b) Vorticity contour at t/T = 10.10. (c) Vorticity contour at t/T = 10.20. (d) Backward FTLE at t/T = 10.00. (e) Backward FTLE at t/T = 10.10. (f) Backward FTLE at t/T = 10.20. (g) Vorticity contour at t/T = 10.25. (h) Vorticity contour at t/T = 10.33. (i) Vorticity contour at t/T = 10.40. (j) Backward FTLE at t/T = 10.25. (k) Backward FTLE at t/T = 10.33. (l) Backward FTLE at t/T = 10.40. (m) Vorticity contour at t/T = 10.50. (n) Backward FTLE at t/T = 10.50. (o) Far-field wake at $t/T = 60$.
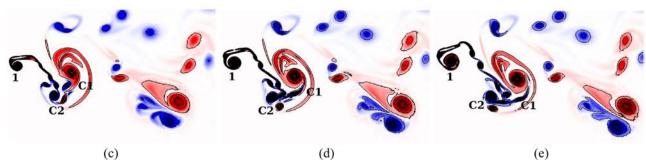
periodic behavior is retained. The chain of events of vortex interactions are similar to the $h = 0.5$ case; for the chosen starting condition here, a downward deflected mode is observed which remains unchanged with time. With further

increase in the plunge amplitude, at $h = 0.8$, the downward deflected vortex street becomes unstable at around $t/T = 15$ and a mode-switching in the vortex street is observed in the far-field after which the wake stabilizes in an upward deflected
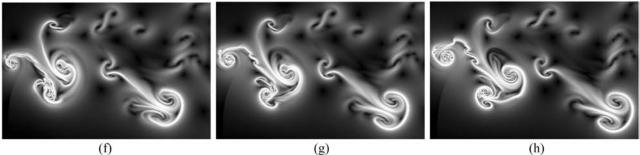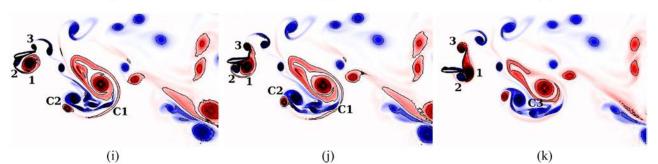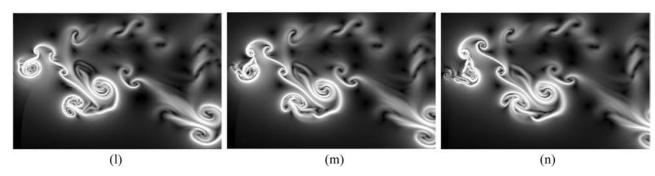
FIG. 15. Quasi-periodic regime: The near-field vorticity dynamics at $h = 0.85$ (up-stroke of 11th cycle). (a) Vorticity contour at t/T = 10.00. (b) Backward FTLE contour at t/T = 10.00. (c) Vorticity contour at t/T = 10.10. (d) Vorticity contour at t/T = 10.20. (e) Vorticity contour at t/T = 10.25. (f) Backward FTLE contour at t/T = 10.10. (g) Backward FTLE contour at t/T = 10.20. (h) Backward FTLE contour at t/T = 10.25. (i) Vorticity contour at t/T = 10.33. (j) Vorticity contour at t/T = 10.40. (k) Vorticity contour at t/T = 10.50. (l) Backward FTLE contour at t/T = 10.33. (m) Backward FTLE contour at t/T = 10.40. (n) Backward FTLE contour at t/T = 10.50.

mode. The near-field vortex interactions at $h = 0.7$ and $h = 0.8$ remain almost similar to that of $h = 0.5$ and the periodicity is still retained.

B. Quasi-periodic regime

As the plunge amplitude is further increased to $h = 0.85$, the periodicity of the near-field wake is seen to be lost. The fundamental vortex mechanisms in this regime are presented for both the up-stroke and the down-stroke of a typical cycle (11th *cycle*) in Figs. 15 and 16, respectively. It is important to discuss both the strokes as unlike the periodic regime

($h = 0.5$) the vortex interactions during the up- and down-strokes are not mirror images of each other. In the periodic regime ($h = 0.5$), a single isolated vortex emerged in the trailing-edge wake in every half-cycle (their signs were opposite in the consecutive half-cycles) constructing a periodic reverse Kármán vortex street. In this second case, one vortex couple having equal strength partners, with downward or upward self-induced translational velocity (depending on the starting condition), is seen to emerge after every cycle. However, there are slight deviations in their strengths as well as in their time of emergence from one cycle to another. This
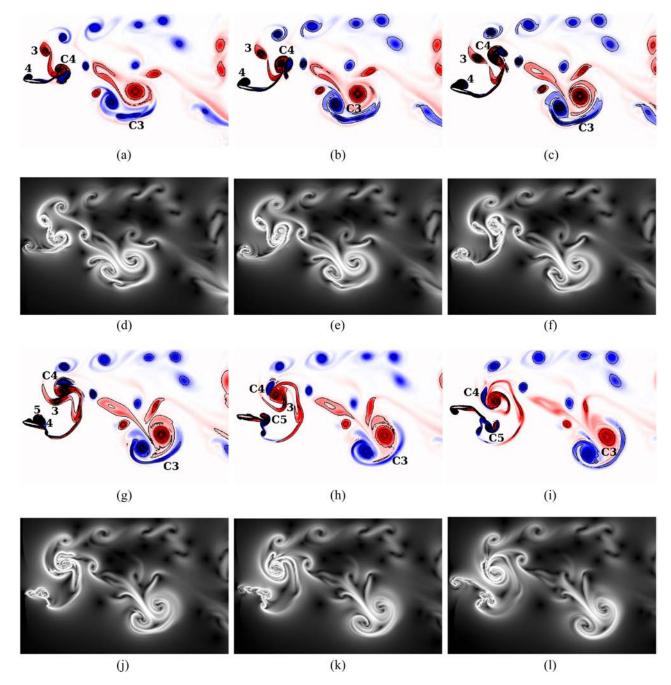

FIG. 16. Quasi-periodic regime: The near-field vorticity dynamics at $h = 0.85$ (down-stroke of 11th cycle). (a) Vorticity contour at $t/T = 10.58$. (b) Vorticity contour at $t/T = 10.67$. (c) Vorticity contour at $t/T = 10.75$. (d) Backward FTLE contour at $t/T = 10.58$. (e) Backward FTLE contour at $t/T = 10.67$. (f) Backward FTLE contour at $t/T = 10.75$. (g) Vorticity contour at $t/T = 10.83$. (h) Vorticity contour at $t/T = 10.90$. (i) Vorticity contour at $t/T = 11.00$. (j) Backward FTLE contour at $t/T = 10.83$. (k) Backward FTLE contour at $t/T = 10.90$. (l) Backward FTLE contour at $t/T = 11.00$.
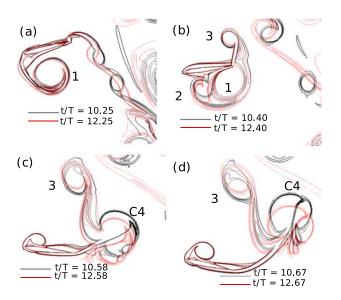
FIG. 17. Quasi-periodic regime: Comparison of leading-edge separation between 11th and 13th cycles.

structure can be considered to be the main building block of the quasi-periodic wake. The slight difference in the time (in other words, a phase difference) could be primarily attributed to a phase lag in the leading edge separation from one cycle to another. This is one of the main architects behind the loss of periodicity in the near-field and in turn for making the wake quasi-periodic. This is discussed in more detail in the following.

At the beginning of the up-stroke (of the 11th cycle), two vortex couples "C1" and "C2" along with a growing LEV "1" are observed in the frame as the primary vortex structures [Fig. 15(a)]. As the airfoil moves upward, the vortex couples "C1" and "C2," formed during the previous cycle, come closer and interact while convecting downstream. The counter clock-wise component of "C1" and the clock-wise component of "C2" integrate to form a couple "C3" which would advect with a downward self-induced velocity during the next half-cycle [Fig. 16(i)]. The weaker counterpart of "C1," that was left behind, gets deformed and partially merged to the clock-wise component of "C3." Whereas, the weaker
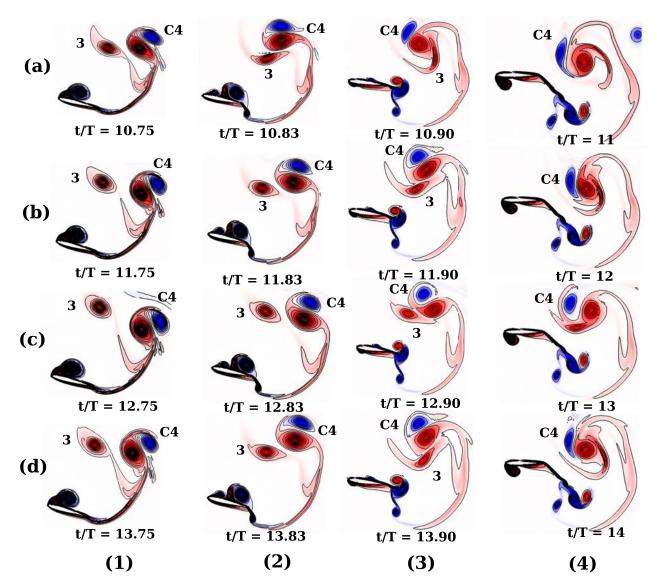

FIG. 18. Quasi-periodic regime: Comparison of LEV-TEV interactions for last quarter of (a) 11th cycle, (b) 12th cycle, (c) 13th cycle, and (d) 14th cycle.

counterpart of "C2" remains as a small isolated vortex in the field. At the same time, a counter clock-wise LEV "1" grows and sheds from the leading edge [Figs. 15(c) and 15(d)]. However, it is seen to reattach itself later at the trailing edge [Fig. 15(j)]. In the mean time, a weak clock-wise vortex ("2") is also formed that convects towards the trailing edge and forms couple "C4" with reattached "1" having unequal counterparts [Fig. 15(k)]. Hence by the end of the upstroke, formation of a strong couple "C3" is initiated which would get completed in the next half-cycle (down-stroke). Also, couple "C4" gets formed that would play an active role in the following upstroke and behave like couple "C1" of the present cycle. TEV "3" is formed which would also take part in vortex interactions in the next half-cycle.

The down-stroke looks different from the up-stroke unlike the periodic case (see Fig. 16). The couple "C4" traverses a circular path in a counter clock-wise trajectory due to the influence of its stronger component and eventually comes near the TEV "3" [Fig. 16(c)]. Subsequently, *partial merging* takes place between the counter clock-wise component of "C4" and "3" [Figs. 16(g)–16(i)]. Formation of "C4" that depends on LEV "1" and "2" suffers a time delay from one cycle to another due to a small time delay in the onset of separation of "1." This also affects the interactions of "C4" and "3" from one cycle to another (will be discussed in more detail later in this subsection). Meanwhile, LEV "4" grows and travels over the upper surface towards the trailing edge [Fig. 16(g)] and subsequently forms a couple "C5" with the secondary vortex structure "5" [Fig. 16(h)]. In the next cycle, "C5" would act like "C2" (upstroke) and "C4" and "C5" will subsequently form a couple, the way "C1" and "C2" formed "C3" in the present cycle. However, the strengths and the trajectories of

"C4" and "C5" are not exactly the same as "C1" and "C2" due to the mentioned time delay effect. By the end of the present down-stroke, the formation of "C3" is complete which was initiated in the upstroke (the fundamental vortex structure of the quasi-periodic wake). Because of the earlier phase differences, the fundamental vortex structure would also show slight deviation from one cycle to another, both in its location and strength.

While probing further into the small discrepancies observed between the consecutive cycles, the formation of "C4" and *partial merging* of "C4" and "3" are both found to be delayed from one cycle to another. The delay in this interaction hinders the formation of the strong couple as discussed above, which is the fundamental structure of the quasi-periodic wake. Figure 17 presents the direct comparison of the vortex contours at same phases during 11th and 13th cycles. The small difference in the growth and separation of LEV "1" and its *partial merging* with "2" is clearly visible that brings in the delay in the formation of "C4" and its subsequent dynamics in the flow-field. To see the dynamics of "C4" and "3," the vorticity contours of 11th–14th cycles are examined for the last half of the down-strokes (last quarter of the corresponding cycles) at the same phases in Fig. 18. Four snapshots at these phase locations in time have been referred to as frames (1)–(4) in the figure. The nomenclature of the vortices is consistent with the previous discussion. In frames (1), "C4" and "3" are seen as separate entities before the *partial merging* is initiated. Their relative positions can be compared between the frames (1) for four consecutive cycles. Their distance is seen to gradually increase from the 11th to the 13th cycle that marks the time lag even before the *partial merging* starts. In the rest of the stroke, as the different stages of the merging take place, the
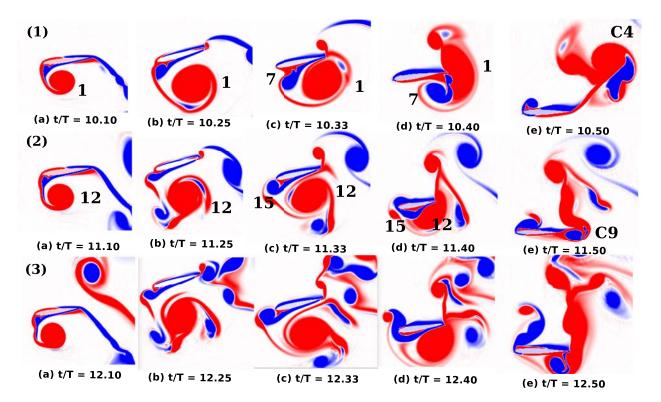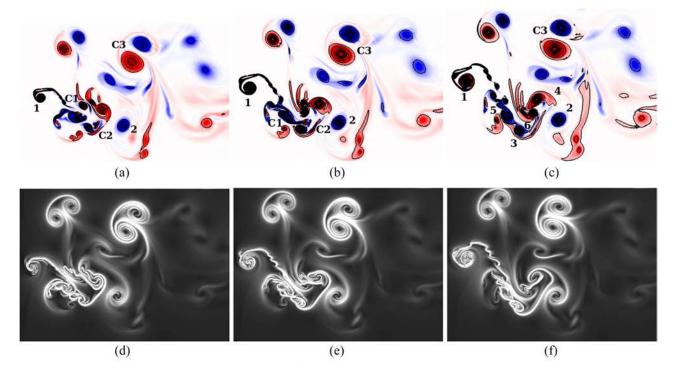

FIG. 19. Chaotic regime: Comparison of leading edge separation in the up-stroke of 11th–13th cycles.

time delay is evident. During the 11th cycle, "C4" and "3" come in contact with each other [see Fig. 18(a–2)], and "3" gets merged partially with the counter clock-wise component of "C4" [Fig. 18(a–3)] that gets completed at the end of the down-stroke [Fig. 18(a–4)]. The same chain of events takes place with a marked time delay at the 12th cycle. A further time delay or phase lag is observed in the 13th cycle. The contact location of "C4" and "3" is seen to be visibly altered

in frames (3) [Fig. 18(c–3)] and *partial merging* between "3" and "C4" is hindered resulting in a distorted "C4" in frames (4) [Fig. 18(c–4)]. The scenario is seen to change in the 14th cycle.

This phase lag upsets the periodic nature of the *partial merging* phenomenon between "C4" and "3" in the consecutive cycles. The resulting couple cannot occupy the exact same location as their other cycle counterparts but stays in the neighborhood. They also attain slightly different trajectories having
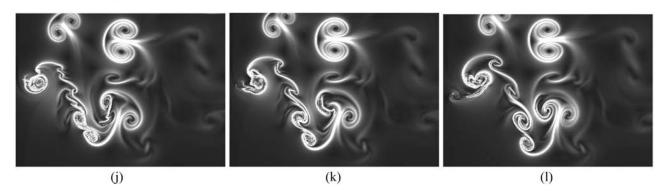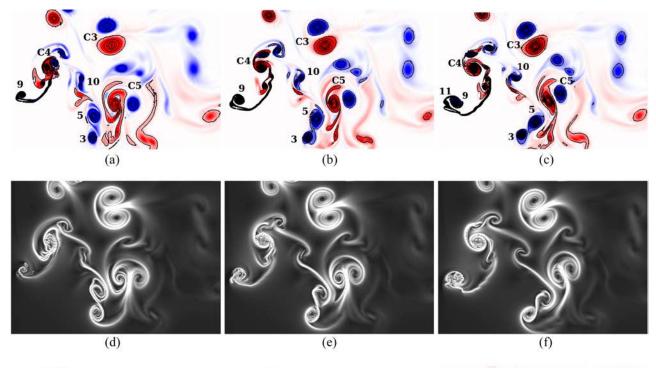

FIG. 20. Chaotic regime: The near-field vorticity dynamics at $h = 1.25$ (up-stroke of 11th cycle). (a) Vorticity contour at $t/T = 10.10$. (b) Vorticity contour at $t/T = 10.20$. (c) Vorticity contour at $t/T = 10.25$. (d) Backward FTLE contour at $t/T = 10.10$. (e) Backward FTLE contour at $t/T = 10.20$. (f) Backward FTLE contour at $t/T = 10.25$. (g) Vorticity contour at $t/T = 10.33$. (h) Vorticity contour at $t/T = 10.40$. (i) Vorticity contour at $t/T = 10.50$. (j) Backward FTLE contour at $t/T = 10.33$. (k) Backward FTLE contour at $t/T = 10.40$. (l) Backward FTLE contour at $t/T = 10.50$.
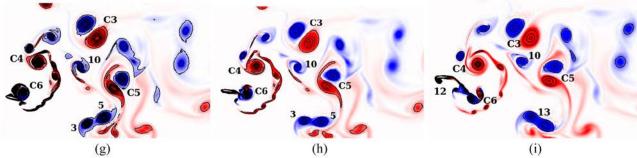
partners of slightly different strengths. As a result of these, the formation of the fundamental vortex couple that should happen due to the collision of "C4" and "C5" is also deviated in the consecutive cycles, marking a quasi-periodic (QP) behavior of the wake.

C. Chaotic regime

In the chaotic regime ($h = 1.25$), the reverse Kármán pattern is completely lost and no regular vortex pattern can be identified. There is clearly no correlation between the flow topology in the consecutive cycles and the flow-field is completely unpredictable in this regime. It is not easy to identify the exact trigger for chaos; however, the LEV behavior is seen to be the starting point. Unlike the QP case, its development and shedding patterns differ significantly from one cycle to another and the unpredictable leading edge separation plays a pivotal role in making the wake aperiodic. In order to examine this closely, the chronology of the LEV formation and
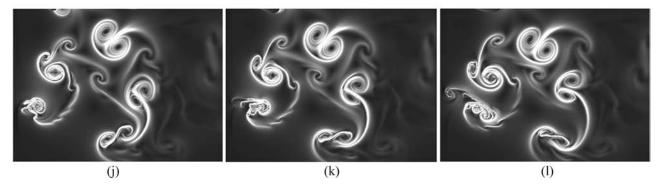

FIG. 21. Chaotic regime: The near-field vorticity dynamics at $h = 1.25$ (down-stroke of 11th cycle). (a) Vorticity contour at $t/T = 10.58$. (b) Vorticity contour at $t/T = 10.67$. (c) Vorticity contour at $t/T = 10.75$. (d) Backward FTLE contour at $t/T = 10.58$. (e) Backward FTLE contour at $t/T = 10.67$. (f) Backward FTLE contour at $t/T = 10.75$. (g) Vorticity contour at $t/T = 10.83$. (h) Vorticity contour at $t/T = 10.90$. (i) Vorticity contour at $t/T = 11.00$. (j) Backward FTLE contour at $t/T = 10.83$. (k) Backward FTLE contour at $t/T = 10.90$. (l) Backward FTLE contour at $t/T = 11.00$.

shedding for three consecutive cycles (11th–13th) are presented in Fig. 19 (during upstrokes). The implication of leading-edge separation on subsequent vortex interaction behavior in the near-field is examined next and is presented for two representative cycles (11th and 12th) in terms of the vorticity contours and the corresponding Lagrangian coherent structures in Figs. 20–23. The nomenclature of the vortices is kept the same in Figs. 19–23.

At the beginning of the upstroke of the 11th cycle, a counter clock-wise LEV "1" grows and gets shed from the leading edge. It reattaches at the trailing edge and forms

a couple "C4" with the smaller clock-wise secondary vortex structure "7" [see Figs. 19(1–a)–19(1–e)]. This changes drastically in the immediate next cycle. In the 12th cycle, the primary LEV (marked as "12") sheds from the leading edge and interacts differently with the already shed clock-wise secondary structure. As a result, part of the LEV is seen to get separated and the remaining part reattaches at the trailing edge with a significant time delay [Figs. 19(2–b) and 19(2–c)]. In addition, a second structure "15" roles up in the leading edge [frame (d)]. The shedding of "12" takes place from the trailing edge but as a much distorted structure [frame (e)],
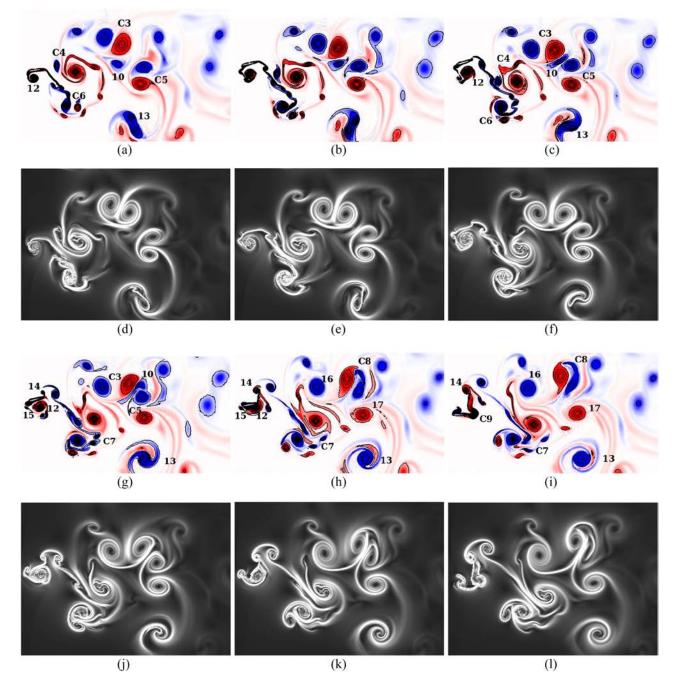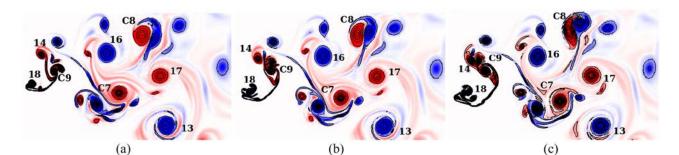

FIG. 22. Chaotic regime: The near-field vorticity dynamics at $h = 1.25$ (up-stroke of 12th cycle). (a) Vorticity contour at $t/T = 11.10$. (b) Vorticity contour at $t/T = 11.20$. (c) Vorticity contour at $t/T = 11.25$. (d) Backward FTLE contour at $t/T = 11.10$. (e) Backward FTLE contour at $t/T = 11.20$. (f) Backward FTLE contour at $t/T = 11.25$. (g) Vorticity contour at $t/T = 11.33$. (h) Vorticity contour at $t/T = 11.40$. (i) Vorticity contour at $t/T = 11.50$. (j) Backward FTLE contour at $t/T = 11.33$. (k) Backward FTLE contour at $t/T = 11.40$. (l) Backward FTLE contour at $t/T = 11.50$.
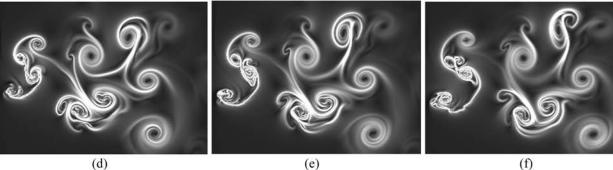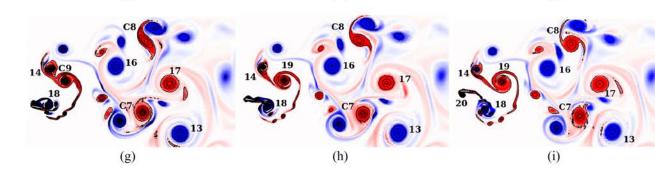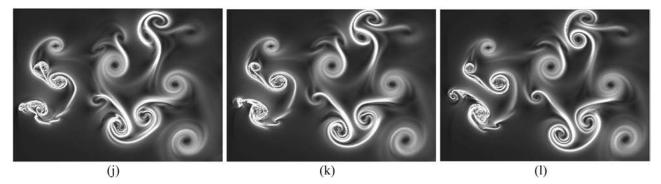
FIG. 23. Chaotic regime: The near-field vorticity dynamics at $h = 1.25$ (down-stroke of 12th cycle). (a) Vorticity contour at $t/T = 11.58$. (b) Vorticity contour at $t/T = 11.67$. (c) Vorticity contour at $t/T = 11.75$. (d) Backward FTLE contour at $t/T = 11.58$. (e) Backward FTLE contour at $t/T = 11.67$. (f) Backward FTLE contour at $t/T = 11.75$. (g) Vorticity contour at $t/T = 11.83$. (h) Vorticity contour at $t/T = 11.90$. (i) Vorticity contour at $t/T = 12.00$. (j) Backward FTLE contour at $t/T = 11.83$. (k) Backward FTLE contour at $t/T = 11.90$. (l) Backward FTLE contour at $t/T = 12.00$.

compared to Fig. 19(1–e). At the same time, "15" forms a weak couple "C9" with a small part of the shed LEV at the trailing edge [Fig. 19(2–e)]. Overall, in this 12th cycle, the formation of the vortex couple is notably disrupted and a pattern completely different from the 11th cycle is observed in the near-field. In the subsequent cycles, the leading edge separation process becomes even more complicated as is evident from the rest of the frames of Fig. 19. This cycle-wise strong difference provides the first trigger to bring chaos in the wake.

The above discussed discrepancy is propagated in the down-stream from one cycle to another strongly altering the subsequent near-field interactions compared to the previous cycles. It is also characterized by multiple vortex interactions which do not repeat themselves in consecutive cycles. Unlike the earlier regimes, in this case the vortex structures *translate*, *merge*, and undergo *collisions* giving birth to rapidly moving vortex couples spontaneously. They collide with each other inelastically forming new couples at any arbitrary location while freely moving in the wake, and all these activities help

sustain the aperiodicity. As a result, the near-field lacks any fundamental structure unlike the periodic and quasi-periodic regimes.

The effect of aperiodic leading edge separation gradually propagates to the entire wake. The first step in this process is the LEV-TEV interactions. As can be seen in Fig. 21, after getting shed from the trailing edge, "C4" traverses in a counter clock-wise trajectory during the down-stroke of the 11th cycle. It is seen to come close to another couple "C6" and *collide inelastically* with it resulting in a new strong couple "C7" [Fig. 22(g)]. Contrastingly in the 12th cycle, formation of the "C4-like" vortex couple at the end of the up-stroke itself is disrupted. Instead, only a weak couple "C9" is seen to shed from the trailing edge and large part of LEV "1" is shed as a separate counter clock-wise entity "14" [Fig. 23(a)],

which eventually undergoes an *inelastic collision* with "C9" [Figs. 23(b) and 23(c)]. Finally, "C9" remains as an isolated vortex "19"; see Fig. 23(g). Hence, any possibility of a subsequent formation of "C7-like" strong couple (as was seen in the 11th cycle) is lost. With this, the discrepancy in the LEV separation pattern has now propagated to the LEV-TEV interaction behavior.

Thus initiated, aperiodicity sustains through a series of rapid irregular interactions that take place among the near-field vortices one after another in a quick succession. These events prevent the formation of an organized wake. These interactions are spontaneous and are completely unpredictable without any regularity in their sequence of occurrence.

For the sake of illustration, cycle 11 and 12 are chosen (please refer to Figs. 20–23). At the start of the up-stroke of
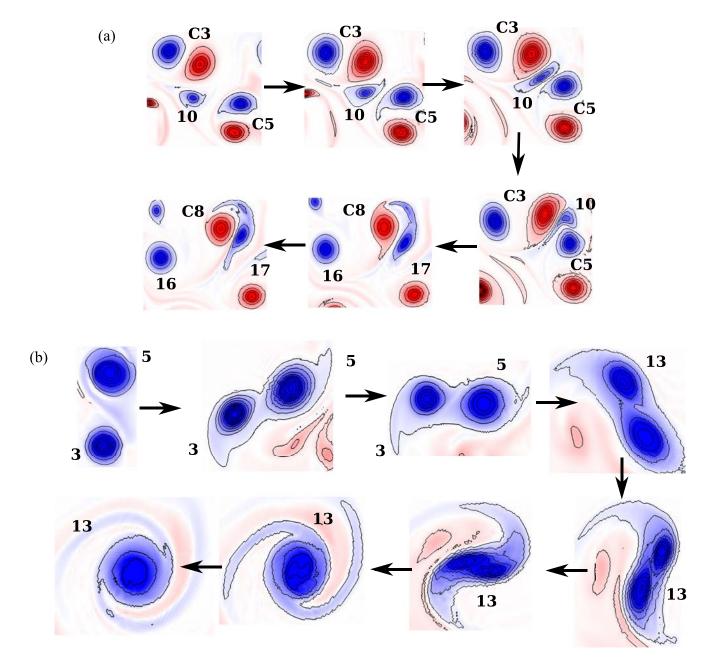

FIG. 24. Typical vortex interaction mechanisms observed in the chaotic flow-field. (a) Collision of vortex couples and change of partner. (b) Vortex merging phenomenon of two co-rotating vortices with equal strengths.

the 11th cycle, two couples "C1" and "C2" are seen to closely interact with each other as seen in Fig. 20(a) (recall that for the quasi-periodic case only a single strong couple was active), which were formed due to LEV-TEV interactions in the previous cycle (not shown here). The couple "C1" moves faster and collides with "C2" due to its higher self-advection velocity. This is an *inelastic collision*, in which they are separated into isolated vortices ("3," "4" and "5," "6") [Fig. 20(c)]. Counter clock-wise vortices "4" and "6" undergo a *complete merging* and form "8" [Figs. 20(g)–20(i)]; "8" is seen to form a couple "C5" with existing vortex "2" [Fig. 21(a)]. Clockwise "3" and "5" also undergo a *complete merging* and eventually form a single vortex "13" having uniform contribution from each [see Figs. 21(a)–22(i)]. Note that this process starts in cycle 11 and extends into cycle 12. Such random interactions and formations continue to happen in the flow-field; couple "C5" comes close to existing couple "C3" and together undergo an *inelastic collision* with an isolated vortex "10" [Fig. 22(b)] and forms a new couple "C8" through the *partner exchange* process. During this process, the isolated vortex 10 gets deformed and gets added to the clock-wise component of "C8" [Figs. 22(g) and 22(h)]. To illustrate further, two important interaction processes, the *partner exchange* between "C3" and "C5" and the *complete merging* process between "3" and "5," are shown in a step by step manner in Figs. 24(a) and 24(b), respectively. This gives a glimpse of the myriad fundamental interaction mechanisms that take place in the flow-field during a typical chaotic cycle which happen in an irregular fashion, thus sustaining the aperiodic behavior. It is also evident from a comparison of Figs. 22 and 23 with Figs. 20 and 21 that the vortex interaction behavior of cycle 12 has no resemblance to the chain of events of cycle 11.

Thus, the aperiodic trigger that was provided by the leading-edge separation (and followed by the LEV-TEV interactions) has now propagated downstream and the entire flow-field has become aperiodic through various vortex interactions. Chaos is sustained by the generation of fast moving free couples that undergo inelastic collisions with others which in turn increases the width of the wake significantly. The exact same chain of events is never seen to repeat in other cycles, which makes the flow patterns irregular and unrepeatable. The fundamental vortex interactions (defined at the beginning of the subsection) do remain present in consecutive cycles, but in different sequences and locations. Although some of the fundamental mechanisms, such as *vortex merging*, *vortex shredding*, etc., were also seen to occur in the periodic and quasi-periodic regimes, they took place either strictly in a periodic manner or with a slight delay from one cycle to the other. On the contrary, these interactions become completely erratic in the chaotic regime.

It should be noted that the results presented here are specific to the chosen kinematics and profile. However, small change in the shape of the profile (e.g., small alteration in the thickness) cannot hinder chaos (based on preliminary numerical investigations not presented here); the LEV trigger for aperiodicity and the fundamental vortex interaction mechanisms like merging, splitting, shredding, spontaneous generation of vortex couples, their mutual collisions, etc., that sustain chaos in the flow-field also remains intact. However, the chaotic

flow-field may look qualitatively different as the fundamental vortex interactions in the far-field occur in different sequences and locations. The same is true for slight changes in the kinematic parameters, like small phase difference between pitch and plunge motions.

V. CONCLUSIONS

In the present paper, the flow past a sinusoidally pitching-plunging airfoil has been investigated. A transition in the flow pattern from periodic to chaotic has been observed with an increase in the plunge amplitude (h) or equivalently the amplitude based Strouhal number (St_A). The flow topology is seen to become chaotic through a quasi-periodic route at higher plunge amplitudes. Three distinct dynamical states, namely, periodic, quasi-periodic, and chaotic have been conclusively established qualitatively as well as quantitatively using robust tools from dynamical systems theory. Thereafter, the underlying vortex interactions, that take place in the unsteady flow-field that provide the onset of a quasi-periodic transition and trigger and sustain chaos in the wake, are investigated. Discrepancy in the leading-edge separation pattern from one cycle to another is found to be the main trigger behind the aperiodic transition in the flow-field. To the best of our knowledge, investigation of the transitional dynamics in the flapping flow-field by probing the role of the fundamental vortex interactions has not been reported earlier in the literature.

The scope of the present analysis is limited to 2D and it aims to establish the role of fundamental vortex interactions behind the chaotic transition in the high Strouhal number regime for a 2D flow-field. It can be expected that the present results for chaos could also be valid in the corresponding 3D field in a broad sense, as the literature[15] suggests that the 3D flow dynamics are able to retain chaos for the high amplitude and low frequency flapping cases as in the present study.

Moreover, existence of chaos is not affected by small changes in the airfoil profile (e.g., slight alteration in thickness) or kinematic parameters (e.g., introduction of small phase gaps between plunge and pitch). The LEV trigger for aperiodicity and the fundamental vortex interaction mechanisms (merging, splitting, shredding, spontaneous generation of vortex couples, their mutual collisions, etc.) that sustain chaos in the flow-field also remain intact. However, these small changes in the input conditions do provide additional disturbances which can be termed as difference in initial conditions, following the terminology of dynamical systems theory. Different initial conditions during chaos can result in very different system outcomes (despite all being chaotic). In other words, they result in very different looking flow-fields during chaos where all the fundamental vortex interaction mechanisms though are present occur at different space and time (sequence and location of events become different). However, this argument cannot be extended for drastic changes in the said input conditions. LEV behavior itself can be drastically different during a large change in airfoil geometry, kinematic phase angle, or Reynolds number which demands a detailed study in the concerned parametric range.

[1] M. F. Platzer, K. D. Jones, J. Young, and J. S. Lai, "Flapping wing aerodynamics: Progress and challenges," AIAA J. **46**, 2136–2149 (2008).

[2] T. J. Mueller, *Fixed and Flapping Wing Aerodynamics for Micro Air Vehicle Applications* (AIAA, 2001), Vol. 195.

[3] S. A. Ansari, N. Phillips, G. Stabler, P. C. Wilkins, R. Żbikowski, and K. Knowles, "Experimental investigation of some aspects of insect-like flapping flight aerodynamics for application to micro air vehicles," Exp. Fluids **46**, 777–798 (2009).

[4] W. Shyy, H. Aono, S. K. Chimakurthi, P. Trizila, C. K. Kang, C. E. S. Cesnik, and H. Liu, "Recent progress in flapping wing aerodynamics and aeroelasticity," Prog. Aerosp. Sci. **46**, 284–327 (2010).

[5] J. S. Lai and M. Platzer, "Jet characteristics of a plunging airfoil," AIAA J. **37**, 1529–1537 (1999).

[6] K. D. Jones, C. M. Dohring, and M. F. Platzer, "Experimental and computational investigation of the Knoller-Betz effect," AIAA J. **36**(7), 1240–1246 (1998).

[7] G. C. Lewin and H. Haj-Hariri, "Modelling thrust generation of a two-dimensional heaving airfoil in a viscous flow," J. Fluid Mech. **492**, 339–362 (2003).

[8] S. Heathcote and I. Gursul, "Jet switching phenomenon for a periodically plunging airfoil," Phys. Fluids **19**(2), 027104 (2007).

[9] M. M. Koochesfahani, "Vortical patterns in the wake of an oscillating airfoil," AIAA J. **27**, 1200–1205 (1989).

[10] T. Schnipper, "Exotic wakes of flapping fins," Ph.D. thesis, Technical University of Denmark, 2010.

[11] K. D. von Ellenrieder and S. Pothos, "PIV measurements of the asymmetric wake of a two dimensional heaving hydrofoil," Exp. Fluids **44**, 733–745 (2008).

[12] R. Godoy-Diana, C. Marais, J. L. Aider, and J. E. Wesfreid, "A model for the symmetry breaking of the reverse Bénard-von Kármán vortex street produced by a flapping foil," J. Fluid Mech. **622**, 23–32 (2009).

[13] M. Yu, H. Hu, and Z. Wang, "Experimental and numerical investigations on the asymmetric wake vortex structures around an oscillating airfoil," in *50th AIAA Aerospace Sciences Meeting Including the New Horizons Forum and Aerospace Exposition* (AIAA, 2012), Vol. 299.

[14] D. Lentink, G. F. Van Heijst, F. T. Muijres, and J. L. Van Leeuwen, "Vortex interactions with flapping wings and fins can be unpredictable," Biol. Lett. **6**, 394–397 (2010).

[15] M. A. Ashraf, J. Young, and J. S. Lai, "Oscillation frequency and amplitude effects on plunging airfoil propulsion and flow periodicity," AIAA J. **50**, 2308–2324 (2012).

[16] T. Kozłowski and H. Kudela, "Transitions in the vortex wake behind the plunging profile," Fluid Dyn. Res. **46**, 061406 (2014).

[17] A. Martín-Alcántara, R. Fernandez-Feria, and E. Sanmiguel-Rojas, "Vortex flow structures and interactions for the optimum thrust efficiency of a heaving airfoil at different mean angles of attack," Phys. Fluids **27**, 073602 (2015).

[18] J. Deng, L. Sun, L. Teng, D. Pan, and X. Shao, "The correlation between wake transition and propulsive efficiency of a flapping foil: A numerical study," Phys. Fluids **28**, 094101 (2016).

[19] D. Lentink, F. T. Muijres, F. J. Donker-Duyvis, and J. L. van Leeuwen, "Vortex-wake interactions of a flapping foil that models animal swimming and flight," J. Exp. Biol. **211**, 267–273 (2008).

[20] P. Blondeaux, L. Guglielmini, and M. S. Triantafyllou, "Chaotic flow generated by an oscillating foil," AIAA J. **43**, 918–922 (2005).

[21] S. Badrinath, C. Bose, and S. Sarkar, "Identifying the route to chaos in the flow past a flapping airfoil," Eur. J. Mech.: B/Fluids **66**, 38–59 (2017).

[22] C. P. Ellington, C. Van Den Berg, A. P. Willmott, and A. L. Thomas, "Leading-edge vortices in insect flight," Nature **384**, 626–630 (1996).

[23] K. Lua, T. Lim, K. Yeo, and G. Oo, "Wake-structure formation of a heaving two-dimensional elliptic airfoil," AIAA J. **45**, 1571–1583 (2007).

[24] K. Streitlien, G. S. Triantafyllou, and M. S. Triantafyllou, "Efficient foil propulsion through vortex control," AIAA J. **34**, 2315–2319 (1996).

[25] J. Anderson, K. Streitlien, D. Barrett, and M. Triantafyllou, "Oscillating foils of high propulsive efficiency," J. Fluid Mech. **360**, 41–72 (1998).

[26] T. Leweke, S. Le Dizès, and C. H. Williamson, "Dynamics and instabilities of vortex pairs," Annu. Rev. Fluid Mech. **48**, 507–541 (2016).

[27] Y. Couder and C. Basdevant, "Experimental and numerical study of vortex couples in two-dimensional flows," J. Fluid Mech. **173**, 225–251 (1986).

[28] G. Haller, "Lagrangian coherent structures," Annu. Rev. Fluid Mech. **47**, 137–162 (2015).

[29] G. Haller, "Distinguished material surfaces and coherent structures in three-dimensional fluid flows," Phys. D **149**, 248–277 (2001).

[30] J. Young and J. C. S. Lai, "Oscillation frequency and amplitude effects on the wake of a plunging airfoil," AIAA J. **42**, 2042–2052 (2004).

[31] Z. C. Zheng and Z. Wei, "Study of mechanisms and factors that influence the formation of vortical wake of a heaving airfoil," Phys. Fluids **24**, 103601 (2012).

[32] C. Liang, K. Ou, S. Premasuthan, A. Jameson, and Z. Wang, "High-order accurate simulations of unsteady flow past plunging and pitching airfoils," Comput. Fluids **40**, 236–248 (2011).

[33] S. Heathcote, Z. Wang, and I. Gursul, "Effect of spanwise flexibility on flapping wing propulsion," J. Fluids Struct. **24**, 183–199 (2008).

[34] W. Tian, A. Bodling, H. Liu, J. C. Wu, G. He, and H. Hu, "An experimental study of the effects of pitch-pivot-point location on the propulsion performance of a pitching airfoil," J. Fluids Struct. **60**, 130–142 (2016).

[35] M. Ashraf, J. Young, and J. Lai, "Reynolds number, thickness and camber effects on flapping airfoil propulsion," J. Fluids Struct. **27**, 145–160 (2011).

[36] M. Yu, Z. Wang, and H. Hu, "Airfoil thickness effects on the thrust generation of plunging airfoils," J. Aircr. **49**, 1434–1439 (2012).

[37] J. Ferziger and M. Peric, *Computational Methods for Fluid Dynamics*, 3rd ed. (Springer-Verlag, Berlin, 2002).

[38] F. M. Bos, B. W. Van Oudheusden, and H. Bijl, "Radial basis function based mesh deformation applied to simulation of flow around flapping wings," Comput. Fluids **79**, 167–177 (2013).

[39] OpenFOAM, "The Open Source CFD Toolbox User Guide" (2013).

[40] F. M. Bos, "Numerical simulations of flapping foil and wing aerodynamics," Ph.D. thesis, TU Delft, 2010.

[41] D. J. Cleaver, Z. Wang, and I. Gursul, "Bifurcating flows of plunging aerofoils at high Strouhal numbers," J. Fluid Mech. **708**, 349–376 (2012).

[42] A. Mackowski and C. Williamson, "Direct measurement of thrust and efficiency of an airfoil undergoing pure pitching," J. Fluid Mech. **765**, 524–543 (2015).

[43] G. Haller and G. Yuan, "Lagrangian coherent structures and mixing in two-dimensional turbulence," Phys. D **147**, 352–370 (2000).

[44] D. Lipinski, B. Cardwell, and K. Mohseni, "A Lagrangian analysis of a two-dimensional airfoil with vortex shedding," J. Phys. A: Math. Theor. **41**, 344011 (2008).

[45] B. M. Cardwell and K. Mohseni, "Vortex shedding over a two-dimensional airfoil: Where the particles come from," AIAA J. **46**, 545–547 (2008).

[46] J. D. Eldredge and K. Chong, "Fluid transport and coherent structures of translating and flapping wings," Chaos: Interdiscip. J. Nonlinear Sci. **20**, 017509 (2010).

[47] P.-F. Lei, J.-Z. Zhang, W. Kang, S. Ren, and L. Wang, "Unsteady flow separation and high performance of airfoil with local flexible structure at low Reynolds number," Commun. Comput. Phys. **16**, 699–717 (2014).

[48] E. Franco, D. N. Pekarek, J. Peng, and J. O. Dabiri, "Geometry of unsteady fluid transport during fluid–structure interactions," J. Fluid Mech. **589**, 125–145 (2007).

[49] J. Chen, J. Zhang, and S. Cao, "Using Lagrangian coherent structure to understand vortex dynamics in flow around plunging airfoil," J. Fluids Struct. **67**, 142–155 (2016).

[50] K. Onu, F. Huhn, and G. Haller, "LCS tool: A computational platform for Lagrangian coherent structures," J. Comput. Sci. **7**, 26–36 (2015).

[51] J. D. Farmer, "Chaotic attractors of an infinite-dimensional dynamical system," Phys. D **4**, 366–393 (1982).

[52] B. R. Noack and F. Obermeier, "A chaos-theoretical investigation of the wake behind a cylinder," Z. Angew. Math. Mech. **71**, 428 (1991).

[53] N. Marwan, M. Carmen Romano, M. Thiel, and J. Kurths, "Recurrence plots for the analysis of complex systems," Phys. Rep. **438**, 237–329 (2007).

[54] J. D. Farmer and J. J. Sidorowich, "Predicting chaotic time series," Phys. Rev. Lett. **59**, 845 (1987).

[55] M. T. Rosenstein, J. J. Collins, and C. J. De Luca, "A practical method for calculating largest Lyapunov exponents from small data sets," Phys. D **65**, 117–134 (1993).

[56] D. Ruelle, "What is a strange attractor?," Not. Am. Math. Soc. **53**, 764–765 (2006).

[57] F. Takens, *Detecting Strange Attractors in Turbulence* (Springer, 1981).

[58] A. M. Fraser and H. L. Swinney, "Independent coordinates for strange attractors from mutual information," Phys. Rev. A **33**, 1134 (1986).

[59] M. B. Kennel, R. Brown, and H. D. Abarbanel, "Determining embedding dimension for phase-space reconstruction using a geometrical construction," Phys. Rev. A **45**, 3403 (1992).

[60] J.-P. Eckmann and D. Ruelle, "Ergodic theory of chaos and strange attractors," Rev. Mod. Phys. **57**, 617 (1985).

[61] N. Marwan, "How to avoid potential pitfalls in recurrence plot based data analysis," Int. J. Bifurcation Chaos **21**, 1003–1017 (2011).

[62] P. Freymuth, W. Bank, and M. Palmer, "First experimental evidence of vortex splitting," Phys. Fluids **27**, 1045–1046 (1984).

[63] K. Gustafson and R. Leben, "Robust multigrid computation and visualization of separation and vortex evolution in aerodynamic flows," in *Proceedings of the 1st National Fluid Dynamics Congress* (AIAA/ASME/SIAM/APS, 1988), pp. 174–184.